



HAL
open science

Quantification of the bone lacunocanalicular network from 3D X-ray phase nanotomography images

Boliang Yu, Alexandra Pacureanu, Cecile Olivier, Peter Cloetens, Françoise
Peyrin

► **To cite this version:**

Boliang Yu, Alexandra Pacureanu, Cecile Olivier, Peter Cloetens, Françoise Peyrin. Quantification of the bone lacunocanalicular network from 3D X-ray phase nanotomography images. *Journal of Microscopy*, 2021, 282 (1), pp.30-44. 10.1111/jmi.12973 . hal-03705692

HAL Id: hal-03705692

<https://hal.science/hal-03705692>

Submitted on 3 Oct 2023

HAL is a multi-disciplinary open access archive for the deposit and dissemination of scientific research documents, whether they are published or not. The documents may come from teaching and research institutions in France or abroad, or from public or private research centers.

L'archive ouverte pluridisciplinaire **HAL**, est destinée au dépôt et à la diffusion de documents scientifiques de niveau recherche, publiés ou non, émanant des établissements d'enseignement et de recherche français ou étrangers, des laboratoires publics ou privés.

Quantification of the bone lacuno-canalicular network from 3D X-ray phase nano-tomography images

Boliang Yu¹, Alexandra Pacureanu², Cécile Olivier^{1,2}, Peter Cloetens², and Françoise Peyrin^{1,2,*}

¹Univ Lyon, CNRS, INSERM, INSA Lyon, Université Claude Bernard Lyon 1, UJM-Saint Etienne, CREATIS, UMR 5220, U1206, 69621, Lyon, France

²ESRF, the European Synchrotron, 38043 Grenoble, France

Abstract

There is a growing interest in developing 3D microscopy for the exploration of thick biological tissues. Recently, 3D X-ray nano computerized tomography has proven to be a suitable technique for imaging the bone lacuno-canalicular network. This interconnected structure is hosting the osteocytes which play a major role in maintaining bone quality through remodeling processes. 3D images have the potential to reveal the architecture of cellular networks, but their quantitative analysis remains a challenge due to the density and complexity of nanometer sized structures and the need to handle and process large datasets, e.g. 2048³ voxels corresponding to 32 GB per individual image in our case. In this work, we propose an efficient image processing approach for the segmentation of the network and the extraction of characteristic parameters describing the 3D structure. These parameters include the density of lacunae, the porosity of lacunae and canaliculi, and morphological features of lacunae (volume, surface area, lengths, anisotropy etc.). We also introduce additional parameters describing the local environment of each lacuna and its canaliculi. The method is applied to analyze eight human femoral cortical bone samples imaged by magnified X-ray phase nano tomography with a voxel size of 120 nm, which was found to be a good compromise to resolve canaliculi while keeping a sufficiently large field of view of 246 μm in 3D. The analysis was performed on a total of 2077 lacunae showing an average length, width and depth of 17.1 μm x 9.2 μm x 4.4 μm , with an average number of 58.2 canaliculi per lacuna and a total lacuno-canalicular porosity of 1.12%. The reported descriptive parameters provide information on the 3D organization of the lacuno-canalicular network in human bones.

1 Introduction

Osteoporosis is a bone disease characterized by a decrease of bone mass and density. It affects the mechanical properties of bone leading to a high risk of fractures even by minor injury or little knock in some serious cases (Currey, 2005). Moreover, osteoporosis is not only a health problem, but also a social and economic issue. According to the official reports in the European Union (EU), 22 million women and 5.5 million men suffered from osteoporosis in 2010 and there were 3.5 million fragility fractures occurring mainly in the areas of hips, spines and wrists, which represented an economic burden of 37 billion € to the EU (Kanis *et al.*, 2016). Since cortical bone is a frequent site of fracture,

42 knowledge about its 3D structure is important to understand the bone mechanical properties and to
43 decipher the mechanisms of bone fragility (Zebaze *et al.*, 2010).

44 Bone has a hierarchical structure with macro, micro and nano organization, and it is known that
45 all scales are involved in bone strength (Rho *et al.*, 1998). At the cellular scale, the lacuno-canalicular
46 network (LCN) forms a complex interconnected porous system deeply embedded in the mineralized
47 bone matrix (Knothe Tate *et al.*, 2004). Osteocytes, which are the most abundant bone cells, are
48 located within the lacunae. Osteocytes have been identified as important regulators in bone
49 remodeling acting as the activator of NF- κ B ligand (RANKL) for the recruitment of osteoclasts (Jilka
50 & O'Brien, 2016) and producing WNT1 to control bone formation through inactivation and
51 overexpression (Joeng *et al.*, 2017). In the LCN, lacunae function as nodes connected with each other
52 through the canaliculi which host the cytoplasmic processes of osteocytes enabling communication
53 with neighboring bone cells (Florencio-Silva *et al.*, 2015). The LCN supports transport of nutrient
54 and waste products (Bonewald, 2011). The osteocytes are thought to sense local loading and
55 interstitial fluid flow inside bone matrix, and to produce and exchange stimuli signals for the control
56 of bone cell activities (Buenzli & Sims, 2015). Therefore, it is crucial to have tools available to
57 quantify the architecture of the LCN in various conditions to better understand its role in regulating
58 bone maintenance and strength.

59 Because of its complex structure, embedded location and fine scale elements, it remains
60 challenging to investigate the LCN in 3D, and in particular to examine the canaliculi whose diameters
61 are far below the micrometer. 2D imaging techniques such as light microscopy (LM) (Marotti *et al.*,
62 1995, Jordan *et al.*, 2003, Qiu *et al.*, 2006), transmission electron microscopy (TEM) (Rubin &
63 Jasiuk, 2005) and scanning electron microscopy (SEM) (Shah & Palmquist, 2017) have been
64 typically used to observe the LCN. The importance of 3D imaging versus 2D imaging was recently
65 highlighted in a study on age-related changes of the LCN in mouse bone using 3D confocal laser
66 scanning microscopy (CLSM) (Heveran *et al.*, 2018) as in several previous works (Kamioka *et al.*,
67 2001, Repp *et al.*, 2017). Recently multiplexed optical imaging techniques offering several contrasts
68 were also proposed (Kamel-ElSayed *et al.*, 2015, Genthial *et al.*, 2017). Focused ion beam SEM
69 (serial FIB-SEM) (Schneider *et al.*, 2011) can image the LCN with a high precision but it is
70 destructive and restricted to a very limited field of view. In previous works, we showed the feasibility
71 of synchrotron radiation (SR) nano-tomography to image the 3D structure of the LCN at very high
72 and isotropic spatial resolution (Langer *et al.*, 2012, Pacureanu *et al.*, 2012). X-ray ptychographic
73 tomography was first demonstrated in (Dierolf *et al.*, 2010) and recently used to analyze the LCN in
74 rats (Ciani *et al.*, 2018, Sharma *et al.*, 2012, Ciani *et al.*, 2016). However, this technique is limited
75 to a field of view of around 50 microns with long acquisition times.

76 Although the 3D microscopic imaging modalities are booming, there have been very few works
77 addressing the development of image processing tools to segment and analyze such images (Ciani *et*
78 *al.*, 2018, Sharma *et al.*, 2012, Ciani *et al.*, 2016, Heveran *et al.*, 2018). Among the existing general-
79 purpose 3D image processing software, we could not identify any which was suitable to segment and
80 extract quantitative parameters of the LCN from 3D nano-CT images. Despite a profuse literature on
81 image segmentation methods, the particular challenges posed by the morphology, slenderness and
82 organization of canaliculi define a new problem. The canaliculi are vessel-like structures occupying
83 just one or a few voxels in diameter, with regions lacking contrast or presenting discontinuities.
84 Methods proposed in the field of vessel segmentation can be of interest (Sato *et al.*, 1998, Moccia *et*
85 *al.*, 2018), but need to be adapted. Moreover, the extraction of quantitative characteristics is also
86 quite specific to the LCN although general-purpose tools may exist for porous materials. The analysis

87 of osteocyte lacunae has been previously addressed in a number of papers (Mader *et al.*, 2013, Dong
88 *et al.*, 2014a, Heveran *et al.*, 2018), but less work has been devoted to the quantification of canaliculi
89 (Kollmannsberger *et al.*, 2017). In addition, the methods have to be compatible with the large size
90 of the data sets. Even with state of art computers, it remains challenging and time-consuming to
91 handle images larger than 32GB interactively with any software.

92 Thus, the aim of this work is to present a method including image acquisition and data processing
93 to extract 3D quantitative parameters of the LCN in human bone. Imaging was performed using
94 magnified X-ray phase nano computerized tomography (CT) at the beamline ID16A of the European
95 Synchrotron Radiation Facility (ESRF), Grenoble, France (Yu *et al.*, 2018). The setup provides
96 reconstructed volumes 2048^3 with a voxel size of 120nm on a field of view of 246 μm in the three
97 spatial directions. The first step in the analysis workflow is the segmentation of lacunae and
98 canaliculi. Then, quantitative parameters for the assessment of the LCN were calculated based on
99 custom image analysis methods. We also introduce new parameters describing the local environment
100 of each volume of interest. The potential of the methods is demonstrated by the analysis of eight
101 femoral bone samples from female donors, providing information about the spatial distribution of
102 the network. In the present study, we used human bone samples extracted from cadavers without a
103 specific pathology. This is a preliminary study that allowed us to develop a methodology to assess
104 the LCN and will be further used to answer dedicated medical questions, in studies on samples from
105 patients with various conditions, such as osteoporosis or osteoarthritis.

106 **2 Materials and methods**

107 In this section, we first describe the imaged bone samples, and briefly introduce the imaging
108 technique. In the following subsections we present the image processing methods developed to
109 segment the lacunae and canaliculi, and extract quantitative parameters of the LCN as well as the
110 statistical analysis methods.

111 **2.1 Sample description**

112 Eight samples were taken from deceased female donors (between 56 and 95 years old) provided by
113 the Centre du Don des Corps (University Paris 5) and the Department of Anatomy Rockefeller,
114 University Lyon. Except the sex and the age, no other information regarding disease status or
115 medication history was available in accordance with legal clauses stated in the French Code of Public
116 Health Ethics (Cai *et al.*, 2017). Femoral diaphyses were extracted from different parts of these
117 cadaveric subjects and wrapped in gauze soaked with saline to keep hydrated, and stored at -20°C
118 until sample preparation. Rectangular prism shaped samples with cross sections of about $0.4\text{ mm} \times$
119 0.4 mm (height approx. 4 mm) were cut along the endosteal-periosteal direction with a water-cooled
120 diamond precision saw (Presi Mecatome T210, Struers Diamond Cut-off Wheel EOD15, Liphy,
121 Grenoble). We scanned eight samples denoted by A1–A8 and ordered by ages of people.

122 **2.2 Synchrotron radiation nano-CT**

123 All the samples were imaged by magnified X-ray phase nano-CT at the beamline ID16A of the ESRF.
124 The X-ray beam was focused to a $\sim 30\text{ nm}$ size and the sample was positioned in the divergent beam
125 downstream the X-ray focus to record magnified in-line holograms (Hubert *et al.*, 2018). The scanned
126 region was selected about $500\text{ }\mu\text{m}$ below the periosteum, close to a Haversian canal but avoiding the
127 canal itself to optimize the use of the field-of-view.

128 After traversing the sample, the X-ray beam is allowed to propagate before being converted into
129 visible light through a scintillator. Magnified images are recorded by a lens-coupled, 16 Mpixels

130 FReLoN (Fast Readout Low Noise) CCD camera developed at ESRF. The camera was used in
 131 binning mode, yielding 2048×2048 pixels. The beamline is equipped with 2 phased in air undulators
 132 with a period of 22.4 mm and 18.3 mm. The fundamental harmonics are at 11.2 keV and 16.9 keV.
 133 In order to work at 33.6 keV, the third harmonic of the U22.4 is used. A multilayer monochromator
 134 and multilayer coated Kirkpatrick-Baez mirrors are used to obtained a focused beam with a
 135 monochromaticity $\Delta E/E=10^{-2}$.

136 Table 1: Experimental parameters of the beamline ID16A

Undulator	Energy	Dose	Exit window	Scintillator	Detector	Exposure time	# projections
U22.4	33.6 keV	1.4 MGy	Polycrystalline diamond window (500 μm)	GGG:Eu 23 μm	FReLon E2V 16 M	0.5 s	2000
U18.3	17.05 keV	2.1 MGy				0.35 s	1800

137
 138 A piezo-driven short-range hexapod stage, operated under vacuum, provides accurate position
 139 control during the tomographic rotation (Villar *et al.*, 2018). Each sample was scanned at four
 140 different focus-to-sample distances, which was shown to provide the best image quality for such
 141 samples, see Fig. 1 (Yu *et al.*, 2018). The beam energy was 17 keV and 33.6 keV during different
 142 data collection sessions. For each distance, 1800 or 2000 projections were recorded over the angular
 143 range of 180° . The information on the beamline and the experimental parameters is summarized in
 144 Table 1.

145 After data acquisition, phase retrieval was performed using an extended Paganin’s method
 146 followed by iterative optimization and the formula in the Frequency domain is shown as following
 147 (Yu *et al.*, 2018):

148
$$\tilde{\varphi}(\mathbf{f}) = \frac{1}{2} \cdot \frac{\delta_n}{\beta} \cdot \frac{\tilde{I}_{D_k}(\mathbf{f}) - \delta_{Dirac}(\mathbf{f})}{\cos(\pi\lambda D_k \|\mathbf{f}\|^2) + \frac{\delta_n}{\beta} \sin(\pi\lambda D_k \|\mathbf{f}\|^2)}. \quad (1)$$

149 where δ_n is the refractive index decrement, β the absorption index, λ the wavelength, D_k the
 150 propagation distance, $\tilde{I}_{D_k}(\mathbf{f})$ the Fourier transform of the intensity image and $\delta_{Dirac}(\mathbf{f})$ the Dirac
 151 function.

152 Subsequently, standard Filtered Back-Projection (FBP) was used for tomographic reconstruction
 153 from the phase maps, using the ESRF implementation of PyHST2 (Mirone *et al.*, 2014). The
 154 reconstructed volumes were made of 2048^3 voxels with a cubic voxel size of 120 nm, yielding a field
 155 of view of 246 μm in the three dimensions. Acquisition time for a complete dataset (i.e. with 4
 156 propagation distances) was approximately 4 hours.

157 All the processing programs in this work were run on the HPC cluster available at the ESRF
 158 using the OAR batch scheduler. The CPU of the used nodes on the cluster was an Intel(R) Xeon(R)
 159 CPU E5-2670 v2 @ 2.50GHz. We used 20 cores (10 per socket) in total to run the segmentation
 160 programs.

161 2.3 Image segmentation

162 The analysis of the LCN requires to segment both the lacunae and the canaliculi. The segmentation
 163 has to be tailored to match the morphological specificities of the lacunae and the thin canaliculi, and
 164 to cope with the noise inherent to the imaging approach. Moreover, we have to design a segmentation
 165 method which can cope with large image sizes, i.e. 32 GB per volume. In order to exploit fully the
 166 knowledge encoded in the images, our aim is to process the entire 3D volume over the entire field

167 of view instead of a cropped volume of interest (VOI). Even with state of art computers, it remains
168 challenging and time-consuming to handle 32 GB images interactively with any software. Thus, we
169 chose to develop codes that could be run offline without user interaction on series of images. Our
170 programs are written in C++ based on the open-source ITK library. The workflow of the
171 segmentation procedure is summarized in Fig. 2, where the top and bottom lines respectively
172 illustrate the segmentation of lacunae and canaliculi which are merged to get the segmented LCN.
173 All image processing steps were done in 3D, and not slice by slice.

174 2.3.1 Segmentation of lacunae

175 The aim of this step is to obtain a binary volume of the lacunae only. The dynamic range of our
176 images, corresponding to the map of $\frac{2\pi\delta}{\lambda}$ (δ the refractive index decrement and λ the wavelength)
177 (Yu et al., 2018), was in the range between 0 and 700 with a contrast to noise ratio around 25 for
178 lacunae. Thus, lacunae are well-contrasted and well-defined objects with a typical ellipsoidal shape.
179 The main issue is that they are connected to each other via the small canaliculi channels. The
180 segmentation of lacunae was based on simple thresholding and filtering methods adapted from a
181 previous work devoted to process absorption SR micro-CT images at 300 nm (Dong et al., 2014a).
182 In the first step, a median filter with a radius of 10 voxels was applied to remove canaliculi while
183 preserving lacunae. Then, we used hysteresis thresholding to segment the lacunae from the images.
184 This method involves two thresholds: the lower threshold is the so-called “hard” threshold, which
185 extracts the voxels of lacunae with high confidence; the other one is a higher threshold, called the
186 “weak” one, which is used to refine the segmentation. The voxels with gray values between two
187 thresholds are assigned to the object if they are connected to the high confidence voxels with respect
188 to the 26-adjacency. The threshold values were adapted from the histograms of each volume. The
189 low threshold was in the middle of two peaks in the histogram and the high threshold at the front
190 edge of the second peak. Finally, portions of Haversian canals that could be included in the
191 segmentation were eliminated after connected component analysis by removing the largest
192 components (threshold of 1 200 000 voxels in our case).

193 2.3.2 Segmentation of canaliculi

194 Compared to lacunae, the segmentation of canaliculi is more difficult due to their slenderness, the
195 diameter of canaliculi being estimated in a range between 100–500 nm (Varga *et al.*, 2015). This
196 problem presents some similarities, although not completely equivalent, with the segmentation of
197 vascular networks in medical imaging. In this context, sophisticated image processing methods have
198 been proposed, summarized within two reviews on the topic (Lesage *et al.*, 2009, Moccia et al.,
199 2018). They include a large variety of techniques such as feature extraction and classification, region
200 growing methods, active contours (snake or level sets) and tracking approaches. However, there are
201 still no universally valid segmentation methods; each approach needs to be substantially adapted to
202 the anatomical structure and to the characteristics of the image in terms of noise, contrast and spatial
203 resolution. Moreover, many sophisticated methods are computationally prohibitive when applied to
204 large 3D images. We previously investigated an advanced tracking approach method based on
205 minimal path and geodesic voting to segment SR micro-CT images acquired at 300 nm (Zuluaga *et*
206 *al.*, 2014). This method used the centroids of lacunae as starting-points of a fast-marching front
207 propagation while the endpoints are chosen as the edge points from each segmented region after
208 Voronoi tessellation. However, the application of this method was not suitable to the higher
209 resolution images used here, as it only returns single voxel thickness of canaliculi and the
210 computational costs are too heavy to enable processing of large data sets. We have thus resorted to

211 a more efficient method based on the shape priors of canaliculi. The method that we propose here is
 212 using a popular filter developed in the context of vessel segmentation, which is dubbed *vesselness*
 213 (Sato et al., 1998). However, this 3D line enhancement filter combined with thresholding is not
 214 sufficiently precise in our case, thus we introduce a second step based on a customized region
 215 growing approach.

216 The *vesselness* enhancement filter uses the eigenvalues of the local Hessian matrix to extract
 217 local shape parameters and enhance slender, elongated structures (Sato et al., 1998, Pacureanu, 2012).
 218 Computation of the Hessian matrix involves the second-order partial derivatives of the image, which
 219 are sensitive to noise. For this reason, smoothing of the image with a 3D Gaussian function of
 220 standard deviation σ was included in the calculation. The three eigenvalues of the Hessian matrix
 221 which were calculated for all voxel positions $\mathbf{x} = (x, y, z)$, are then sorted in ascending order of
 222 magnitude and denoted λ_1, λ_2 and λ_3 ($|\lambda_1| \leq |\lambda_2| \leq |\lambda_3|$) (for simplicity we omit the \mathbf{x} dependency
 223 in the eigenvalues). For the bright tubular structures on dark background which we want to segment
 224 as canaliculi, the eigenvalues should meet the conditions: $|\lambda_1| \approx 0$; $\lambda_1 \ll \lambda_2$; $\lambda_2 \approx \lambda_3$ and both of
 225 them should be negative. If we denote the *vesselness* enhanced image $l(\mathbf{x})$, it can be expressed as
 226 (Sato et al., 1998):

$$227 \quad l(\mathbf{x}) = \begin{cases} \lambda_c \exp\left(\frac{-\lambda_1^2}{2(\alpha_1 \lambda_c)^2}\right), & \lambda_1 \leq 0, \lambda_c > 0 \\ \lambda_c \exp\left(\frac{-\lambda_1^2}{2(\alpha_2 \lambda_c)^2}\right), & \lambda_1 > 0, \lambda_c > 0 \\ 0, & \text{otherwise} \end{cases} \quad (2)$$

228 where $\alpha_1 = 0.5$ and $\alpha_2 = 2$ are two constant parameters chosen based on a previous report by our
 229 group (Pacureanu *et al.*, 2010). Figure 3 illustrates Minimum Intensity Projections (MIPs) of the 3D
 230 volumes at different steps of the process. The MIPs are calculated along the Z-axis by selecting the
 231 minimum intensity value for each XY coordinate from a selected number of slices (here 256). Fig. 3
 232 (b) shows the output of the *vesselness* filter.

233 After this step, the 3D *vesselness* enhanced image is used as input to a region growing method.
 234 The initialization of the region growing starts from a best guess image dubbed the “seed map”. This
 235 binary image is meant to include parts which belong to the sought-after structure with very high
 236 probability, and which will evolve by aggregating new voxels belonging to the target structure. The
 237 initialization process should be automatic and efficient to segment as many target voxels as possible
 238 but avoid other objects having similar features like collagen fibers and speckle noise in our case. We
 239 have determined that by thresholding the *vesselness* map using a rather restrictive criterion we obtain
 240 a binary image containing only voxels belonging to canaliculi. Among various global thresholding
 241 methods, we selected the maximum entropy thresholding method which maximizes the inter-class
 242 entropy (Sahoo *et al.*, 1988). The resulting binary image was used as the seed map of the region
 243 growing method where bright voxels are the starting points of the growth.

244 We chose a region-growing approach that could consider our priors concerning the line structures
 245 to be segmented. Variational region growing (VRG) permits to build a theoretical framework to
 246 formalize the iterative growing process by minimizing a region-based energy function (Pacureanu et
 247 al., 2010, Rose *et al.*, 2010). If we define the 3D image as $f(\mathbf{x})$ in the domain Ω (a subset of the
 248 image), the evolving function can be expressed based on a characteristic function $\varphi_{\mathbf{x}}$:

$$249 \quad \varphi_{\mathbf{x}} = \varphi(\mathbf{x}) = \begin{cases} 1, & \text{if } \mathbf{x} \in \Omega_{\text{in}} \\ 0, & \text{if } \mathbf{x} \in \Omega_{\text{out}} \end{cases}, \quad (3)$$

250 where Ω_{in} is the segmented region in Ω , and $\Omega_{\text{out}} = \Omega \setminus \Omega_{\text{in}}$ the background region.

251 The set of candidate voxels C^n at the iteration n are defined as:

$$252 \quad C^n(\Omega_{in}, \varepsilon) = \{\mathbf{u} \in \Omega_{out}, \mathbf{v} \in \Omega_{in} \mid \|\mathbf{u} - \mathbf{v}\| \leq \varepsilon\}, \quad (4)$$

253 where ε the distance threshold.

254 At each iteration step, we check the candidate voxels belonging to the background Ω_{out} and
 255 connected to the segmented region Ω_{in} . If the new energy function decreases, these voxels are
 256 accepted as objects and we update the characteristic function.

257 If the region-based energy function is noted by $J(\varphi)$, the optimal solution φ^* of the energy
 258 minimization can be expressed as:

$$259 \quad \varphi^* = \operatorname{argmin} J(\varphi_x) \quad (5)$$

260 To compute the solution, we define the time-dependent variation of φ_x as $\Delta_t \varphi$ and estimate the
 261 energy variation $\Delta J(\tilde{\varphi})$ for a small variation $\tilde{\varphi}$ as follows:

$$262 \quad \Delta_t \varphi - c(\varphi) \cdot H(-\Delta J(\tilde{\varphi})) = 0 \quad (6)$$

263 where $c(\varphi) = 1 - 2\varphi_x$ is the switch function, and H the one-dimensional Heaviside function defined
 264 by:

$$265 \quad H(z) = \begin{cases} 1, & \text{if } z < 0 \\ 0, & \text{if } z \geq 0 \end{cases} \quad (7)$$

266 Then, the value of the function φ_x at the iteration $n + 1$ can be given by:

$$267 \quad \varphi_x^{n+1} = \varphi_x^n + c(\varphi_x^n) \cdot H(-\Delta J(\tilde{\varphi}_x^n)) \quad (8)$$

268 Based on the given ‘‘region-independent’’ descriptor k_x Jehan-Besson et al. has defined a general
 269 expression for the region-based energy function (Jehan-Besson *et al.*, 2003):

$$270 \quad J(\Omega_{in}) = \int_{\Omega_{in}} k_x dx \quad (9)$$

271 In our discrete case, we rewrite the energy function as:

$$272 \quad J(\Omega_{in}) = \sum_{x \in \Omega} k_x \cdot \varphi_x^n \quad (10)$$

273 Here, we calculate the energy $J(\tilde{\varphi}^n)$ when the state of a voxel \mathbf{v} is switched to the opposite side.
 274 The characteristic function of this voxel turns:

$$275 \quad \tilde{\varphi}_v^n = 1 - \varphi_v^n \quad (11)$$

276 The other voxels keep the previous states, so we have:

$$277 \quad \tilde{\varphi}_x^n = \varphi_x^n, \quad \text{if } \mathbf{x} \neq \mathbf{v} \quad (12)$$

278 Then, the energy function after switching can be expressed as:

$$279 \quad J(\tilde{\varphi}^n) = k_v \cdot \tilde{\varphi}_v^n + \sum_{x \in \Omega, x \neq v} k_x \cdot \varphi_x^n \quad (13)$$

280 We make an equivalent transformation of this function,

$$281 \quad J(\tilde{\varphi}^n) = k_v \cdot (1 - \varphi_v^n) - k_v \cdot \varphi_v^n + \underbrace{k_v \cdot \varphi_v^n + \sum_{x \in \Omega, x \neq v} k_x \cdot \varphi_x^n}_{J(\varphi^n)} \quad (14)$$

282 Finally, we can obtain the variation of the energy function $\Delta J(\tilde{\varphi}^n)$:

$$283 \quad \Delta J(\tilde{\varphi}^n) = (1 - 2\varphi_v^n) \cdot k_v \quad (15)$$

284 Note that this expression is valid for any region-independent descriptor k_v .

285 This variational formalism can be used for different region-based energy functions such as the
 286 average of gray level (Chan & Vese, 2001) or the estimation of probability distributions (Zhu &
 287 Yuille, 1996). To cope with the complex structure of the LCN, especially with the slender size of
 288 canaliculi, we proposed a region-based energy function which combines information from the 3D
 289 *vesselness* filter map $l(\mathbf{x})$ with information from the original image $f(\mathbf{x})$. $l(\mathbf{x})$ maps the likelihood of
 290 the voxels to belong to a canaliculi, and thus it filters out the lacunae which have ellipsoidal shapes.
 291 In order to reconstruct the entire lacuno-canalicular network, the region-growing is governed by the
 292 *vesselness* map when $l(\mathbf{x})$ has a high value, that is, the considered voxels belong to canaliculi, and
 293 conversely, by the original image $f(\mathbf{x})$ offering strong contrast inside lacunae, when $l(\mathbf{x})$ has a low
 294 value. The energy function is written as:

$$295 \quad J(f, l) = H(f(\mathbf{x}) - \delta)J_f(f) + (1 - H(f(\mathbf{x}) - \delta))J_{f,l}(f, l), \quad (16)$$

296 where

$$297 \quad J_f(f) = \int_{\Omega_{in}} (f(\mathbf{x}) - \mu_{in})^2 d\mathbf{x} + \int_{\Omega_{out}} (f(\mathbf{x}) - \mu_{out})^2 d\mathbf{x}, \quad (17)$$

298 and

$$299 \quad J_{f,l}(f, l) = \int_{\Omega_{in}} G_{\mu_{in}, \sigma_{in}}(f, l) d\mathbf{x} + \int_{\Omega_{out}} G_{\mu_{out}, \sigma_{out}}(f, l) d\mathbf{x}$$

$$300 \quad G_{\mu, \sigma}(f, l) = \frac{1}{\sqrt{2\pi} \sigma} \exp\left(-\frac{(f(\mathbf{x}) - \mu)^2}{2\sigma^2 l(\mathbf{x})}\right) \quad (18)$$

301 where μ_{in} and μ_{out} are the average gray values in the domain Ω_{in} and Ω_{out} of the original image $f(\mathbf{x})$,
 302 σ_{in} and σ_{out} the corresponding standard deviations, H the Heaviside function, δ a threshold value.

303 Then, the variation of the energy function can be calculated by:

$$304 \quad \Delta J(\varphi^{n+1}) = (1 - 2\varphi^n) (\Delta J_f(f) + \Delta J_{f,l}(f, l)) \quad (19)$$

305 where we have

$$306 \quad \Delta J_f(f) = (f(\mathbf{x}) - \mu_{f_{in}})^2 - (f(\mathbf{x}) - \mu_{f_{out}})^2 \quad (20)$$

307 and

$$308 \quad \Delta J_{f,l}(f, l) = \frac{1}{\sqrt{2\pi} \sigma_{f_{in}}} \exp\left(-\frac{(f(\mathbf{x}) - \mu_{f_{in}})^2}{2\sigma_{f_{in}}^2 l(\mathbf{x})}\right) - \frac{1}{\sqrt{2\pi} \sigma_{f_{out}}} \exp\left(-\frac{(f(\mathbf{x}) - \mu_{f_{out}})^2}{2\sigma_{f_{out}}^2 (1-l(\mathbf{x}))}\right) \quad (21)$$

309 Finally, we filtered out the smallest connected components which could be collagen fibers or
 310 noise. The threshold was set to 100 voxels, corresponding to a volume of $0.17\mu\text{m}^3$, after examining
 311 the histogram of the component sizes and the residual noise in the image. Since the segmented image
 312 contains both canaliculi and parts of lacunae as shown in Fig. 3 (d), we subtracted the segmented
 313 lacunae from the result to obtain the binary image of canaliculi only, see Fig. 3 (e).

314

315 **2.4 Quantitative analysis**

316 In this section, we describe the parameters extracted from both the binary lacunae and canaliculi
 317 images.

318 2.4.1 Quantification of lacunae

319 The binary lacunae image was first labeled by using a connected component analysis. The labels
320 were consecutive integer values starting at one, after sorting the objects (lacunae) by decreasing size.
321 We used the 26 connectivity in 3D. The number of lacunae $Lc.N$ was calculated by counting the total
322 number of labels. Let us denote L_n an osteocyte lacuna with label n . For each specific lacuna L_n , its
323 volume $Lc.V$ can be simply computed by summing all the voxels with label n .

324 We used a method based on the second-order central moments to estimate the lengths of three
325 principal axes of each lacuna by fitting it to an ellipsoid as previously described (Dong et al., 2014a).
326 The final length, width and depth ($Lc.L_1$, $Lc.L_2$ and $Lc.L_3$) of the ellipsoid are expressed as a function
327 of the three eigenvalues of the second-order central moment matrix. Besides, we calculated different
328 ratios such as $\frac{Lc.L_1}{Lc.L_2}$ and $\frac{Lc.L_2}{Lc.L_3}$ to assess the anisotropy of the lacunae.

329 We also calculated the intrinsic volumes of lacunae providing interesting characteristics of
330 shapes, such as the surface area $Lc.S$ and the structural model index $Lc.SMI$ of each lacuna,
331 computed by using the Crofton formula (Ohser & Schloditz, 2009).

332 The density of lacunae $\frac{Lc.N}{BV}$ in the whole volume was computed as the number of total lacunae
333 divided by the bone volume while the porosity $\frac{Lc.TV}{BV}$ was equal to the total volume of lacunae in the
334 reconstruction divided by the bone volume.

335 Moreover, we introduce here local parameters computed in the neighborhood of each lacuna, by
336 using the 3D Voronoi tessellation of the images after connected components analysis, see Fig. 4. We
337 calculated the Voronoi diagram associated to the centroids of each lacuna. After this step, we got a
338 partition of the 3D volume into small regions, that we called $Cell$, each of them containing only one
339 lacuna and its canaliculi. Then, we computed the average volume of each Voronoi cell ($Cell.V$) and
340 the local lacunar porosity expressed by the ratio between the average volume of lacuna per Voronoi
341 cell and the average volume of each Voronoi cell ($\frac{Lc.V}{Cell.V}$).

342 2.4.2 Quantification of canaliculi

343 Similarly, we calculated the 3D porosity of canaliculi $\frac{Ca.TV}{BV}$ in the whole volume expressed as the
344 total volume of canaliculi divided by the bone volume. To obtain a local measure, we also computed
345 the local canalicular porosity expressed by the ratio $\frac{Ca.V}{Cell.V}$ between the average volume of canaliculi
346 per cell and the average volume of each cell, and the ratio $\frac{Ca.V}{Lc.V}$ between the average volume of
347 canaliculi and lacunae per cell. Moreover, we calculated the total porosity of the LCN ($\frac{LCN.TV}{BV}$) for
348 the evaluation of the whole network. Besides, to quantify the ramification of canaliculi, we calculated
349 the number of canaliculi per lacuna ($Ca.N$) (Dong et al., 2014b).

350

351 2.5 Statistical analysis

352 We provide the average and standard deviation of all parameters. The correlations between
353 parameters were studied by using the Spearman correlation coefficient (R^2) and the p-value by the
354 Fisher's r to z transformation. These calculations and analysis were performed by Statview® (SAS
355 Institute Inc., Cary, NC, USA). P-values under 0.05 were considered as significant.

360 **3 Results**

361 In this section, we will give the results of the segmentation workflow and the quantitative LCN
362 parameters of the eight samples.

369 **3.1 Segmentation method**

360 Figure 5 illustrates results of the segmentation by the VRG method around three selected lacunae.
361 MIPs are shown for VOIs of $256 \times 256 \times 128$ voxels, corresponding to a physical size of $30.7 \mu\text{m} \times 30.7$
362 $\mu\text{m} \times 15.4 \mu\text{m}$. Figure 5 respectively shows the MIPs of: (a)-(d)-(h) the original reconstructed volume;
363 (b)-(e)-(i) the segmented image by the maximum entropy thresholding; (c)-(f)-(j) the variation region
364 growing method initialized by (b)-(d)-(h). We can see that the latter detects both the lacunae and
365 canaliculi voxels. The red circle regions in Fig. 5 show that the connectivity between some canaliculi
366 is restored after the variational region growing process.

367 We also compared the result of the region growing segmentation to the geodesic voting method
368 previously developed in our group (Zuluaga et al., 2014). We compare the running time of the two
369 methods to segment canaliculi from one reconstructed volume, excluding the pre and post processing
370 before and after the segmentation, and we check the segmented results visually. The variational
371 region growing method needed 830 seconds to finish the process, while the geodesic voting took 17
372 700 seconds, which is 21.3 times longer. Fig. 6 illustrates the segmentation results of the two
373 methods. To improve the visualization, we overlaid the lacunae segmented by the method mentioned
374 in the previous section on a region of $2048 \times 2048 \times 128$ voxels. Figure 6 displays the MIP of (a)
375 the original volume, (b) the LCN segmented by using variational region growing, (c) the LCN
376 segmented by using geodesic voting; (d), (e), (f) are zooms of the MIPs shown in (a), (b) and (c),
377 respectively. We can see that both methods achieve the extraction of canaliculi from the
378 reconstructed volumes. However, when using the geodesic voting, the connectivity between
379 canaliculi is broken in some regions and the thickness of the extracted canaliculi is intrinsically one
380 voxel which is smaller than that of variational region growing, see Fig. 6 (e) and (f), and not
381 representative of the truth at this scale. This observation was confirmed by the computation of the
382 connectivity in one selected volume segmented from both methods. The connectivity is defined as
383 the number of cuts that can be made in an object without breaking it in distinct components. Since it
384 is a number without unit, it is conventionally normalized by the total volume, thus expressed as a
385 density of connectivity in mm^{-3} . The connectivity was derived from the Euler number efficiently
386 computed on discrete grids as described in (Ohser & Schladitz, 2009). The result showed that the
387 connectivity of the network segmented with the VRG method ($4.98 \cdot 10^6 \text{mm}^{-3}$) was about four times
388 that found from the geodesic voting method ($1.21 \cdot 10^6 \text{mm}^{-3}$), showing a better preservation of the
389 integrity of the LCN. In addition, as expected, the geodesic voting method does not permit to quantify
390 the thickness since by construction the canaliculi are restricted to one voxel. These results confirm
391 that the variational region growing method is better suited to segment the canaliculi in the present
392 study, with the additional advantage of being faster.

393 In Fig. 7 (a), we show the MIP along the Y-axis of 100 middle slices from the reconstructed
394 volume of the sample A2 in order to observe the distribution of lacunae surrounding the osteon. The
395 3D visualization of the segmented lacunae and canaliculi rendered by VGStudioMax® is given in
396 Fig. 7 (b).

397

398 **3.2 Quantitative analysis of the LCN in human bone**

399 Here, we report the quantitative LCN parameters extracted from the whole images of the eight human
400 diaphysis bone samples.

401 **3.2.1 Morphometric parameters of lacunae**

402 Table 2 presents the descriptive statistics of lacunae parameters for each sample. Whenever this
403 applies, we provide the mean and standard deviation of the parameter within the sample. For such
404 parameters, the last line of the table provides the mean and standard deviation in all pooled lacunae.
405 In total, we analyzed 2077 lacunae with an average number of lacunae per volume of 259.6. The
406 mean lacunar porosity of 0.78%. The average lacunar volume and surface were respectively 315.7
407 μm^3 and 323.3 μm^2 . The average Voronoi cell volume was found to be 42,000 μm^3 and the average
408 local lacunar porosity was 0.88 %. The average length, width and depth of each lacuna were 17.1
409 μm , 9.2 μm and 4.4 μm , respectively and showed some dispersion within each volume. The
410 anisotropy of the lacunae, described by the ratio between the length and the width, was found to be
411 2.0, the ratio between the width and the depth was found to be 2.2 and the structural model index
412 found to be 3.1.

413 Table 2: Morphometric parameters of lacunae

Sample ID	$Lc.N$	$Lc.TV$ (10^{-5}mm^3)	$Lc.TV/BV$ (%)	$Lc.N/BV$ (10^4mm^{-3})	$Lc.V$ (μm^3)	$Cell.V$ ($10^4 \mu\text{m}^3$)	$Lc.V/Cell.V$ (%)
A1	194	7.6	0.88	2.2	393.4±172.6	5.1±2.8	0.92±0.55
A2	298	9.3	0.81	2.6	311.1±116.6	3.6±1.3	0.98±0.59
A3	347	10.1	0.9	3.1	291.5±108.1	3.1±1.1	1.02±0.49
A4	255	7.2	0.64	2.3	284.1±99.9	4.3±1.6	0.75±0.39
A5	278	8.3	0.77	2.6	298.8±96.4	3.8±1.3	0.86±0.38
A6	229	7.6	0.83	2.5	333.4±132.6	5.1±2.7	0.84±0.53
A7	222	7.6	0.69	2	341.0±168.5	4.6±1.8	0.83±0.47
A8	254	7.8	0.69	2.3	307.0±161.3	4.3±1.5	0.77±0.36
Mean All	259.6	8.2	0.78	2.4	315.7	4.2	0.88
Std. All	44.9	0.9	0.09	0.3	134.8	2.3	0.48

Sample ID	$Lc.S$ (μm^2)	$Lc.L1$ (μm)	$Lc.L2$ (μm)	$Lc.L3$ (μm)	$Lc.L1/Lc.L2$	$Lc.L2/Lc.L3$	$Lc.SMI$
A1	365.8±110.7	19.3±4.7	9.1±2.2	4.7±1.2	2.2±0.8	2.0±0.6	3.1±0.3
A2	334.7±92.8	16.8±4.0	10.0±2.1	4.1±1.0	1.8±0.6	2.6±0.8	3.0±0.4
A3	298.3±77.2	16.9±4.3	8.2±1.8	4.7±1.0	2.2±0.8	1.8±0.5	3.2±0.4
A4	301.9±81.7	15.7±3.6	9.3±2.1	4.3±1.0	1.8±0.6	2.3±0.8	3.0±0.4
A5	317.4±70.0	16.4±3.8	9.3±1.8	4.5±1.0	1.8±0.6	2.2±0.7	3.0±0.4
A6	329.3±91.4	17.2±4.2	9.2±1.9	4.5±1.1	2.0±0.7	2.1±0.6	3.1±0.3
A7	335.6±110.5	17.7±4.8	9.1±2.4	4.6±1.3	2.1±0.8	2.1±0.8	3.1±0.4
A8	323.4±106.5	17.5±5.0	9.1±2.2	4.3±1.0	2.1±0.9	2.2±0.7	3.1±0.4
Mean All	323.3	17.1	9.2	4.4	2	2.2	3.1
Std. All	93.8	4.4	2.1	1.1	0.8	0.7	0.4

415 $Lc.N$ – number of lacunae
416 BV – bone volume (mm^3)
417 $Lc.N/BV$ – density of lacunae (mm^{-3})
418 $Cell.V$ – average volume of each cell (μm^3)
419 $Lc.V/Cell.V$ – local lacunar porosity (%)
420 $Lc.L1$, $Lc.L2$ and $Lc.L3$ – average length, width and depth of lacuna (μm)
421 $Lc.L1/Lc.L2$ and $Lc.L2/Lc.L3$ – average anisotropy of lacuna
422

423 **3.2.2 Morphometric parameters of canaliculi**

424 Similarly, Table 3 reports the morphometric parameters calculated on canaliculi for the eight samples.
425 The average total volume of canaliculi was $3.6 \times 10^{-5} \text{mm}^3$ and the average canaliculi porosity was

426 0.35%. The average volume of canaliculi per cell was $139.3 \mu\text{m}^3$ with the average local canalicular
 427 porosity of 0.37%. In addition, the average ratio between the volume of canaliculi and the lacuna in
 428 the same cell is 45.8%. The average porosity of the complete LCN was 1.12%. Close to the lacuna
 429 surface (at $1.2 \mu\text{m}$), the average number of canaliculi per lacuna was 58.2.

430 Table 3: Morphometric parameters of canaliculi

Sample ID	$Ca.TV$ (10^{-5} mm^3)	$LCN.TV$ (10^{-5} mm^3)	$Ca.TV$ /BV (%)	$LCN.TV$ /BV (%)	$Ca.V$ (μm^3)	$Ca.V$ /Cell.V (%)	$Ca.V/Lc.V$ (%)	$Ca.N$
A1	3.2	10.9	0.37	1.26	166.9±93.9	0.36±0.21	45.1±22.9	67.8±30.1
A2	5.2	14.5	0.46	1.27	175.4±89.8	0.52±0.25	58.4±28.8	71.8±28.9
A3	2.8	12.9	0.25	1.14	80.2±42.1	0.27±0.13	29.4±16.7	49.8±20.3
A4	3.0	10.2	0.26	0.9	116.8±78.4	0.29±0.18	42.6±28.5	51.4±24.2
A5	4.2	12.5	0.39	1.16	149.8±103.6	0.42±0.30	50.4±32.4	62.0±28.1
A6	5.2	12.9	0.57	1.4	228.0±147.5	0.52±0.34	71.7±49.4	59.0±32.7
A7	3.3	10.9	0.3	0.99	148.2±79.7	0.36±0.19	47.0±25.9	60.4±27.9
A8	2.0	9.8	0.18	0.87	79.8±43.5	0.20±0.11	27.9±15.2	46.4±24.0
Mean All	3.6	11.8	0.35	1.12	139.3	0.37	45.8	58.2
Std. All	1.1	1.5	0.12	0.18	99.9	0.25	31.7	28.1

431 $Ca.TV$ – total volume of canaliculi (mm^3) $LCN.TV$ – total volume of the LCN (mm^3)
 432 $Ca.TV/BV$ – porosity of canaliculi (%) $LCN.TV/BV$ – porosity of the LCN (%)
 433 $Ca.V$ – average volume of canaliculi per cell (μm^3) $Ca.V/Cell.V$ – local porosity of canaliculi
 434 $Ca.V/Lc.V$ – ratio between the average volume of canaliculi and lacuna per cell (%)
 435

436 3.2.3 Statistical analysis

437 Table 4 reports the correlation coefficients and p -values of selected quantitative parameters showing
 438 the best correlation ($R^2 > 0.5$ and $p < 0.05$). For instance, the lacunae volume and surface were the
 439 most correlated traducing some homogeneity in shape.

440 Table 4: Spearman correlation between morphologic parameters

Parameter 1	Parameter 2	120 nm	
		R^2	p-value
$Lc.N/BV$	$Cell.V$	0.5390	0.0381
$Lc.TV/BV$	$Lc.V/Cell.V$	0.6840	0.0113
$Lc.V$	$Lc.S$	0.8757	0.0006
$Lc.L1$	$Lc.S$	0.7469	0.0056
$Lc.L2/Lc.L3$	$Lc.SMI$	0.8375	0.0014
$Ca.TV/BV$	$Ca.V/Cell.V$	0.9213	0.0002

441 4 Discussion

442 We presented a dedicated method to measure 3D characteristics of the LCN from X-ray nano-CT
 443 data. The segmentation of lacunae in our images was quite straightforward thanks to their high
 444 contrast ($> 80\%$) and their large size ($\sim 17, 9$ and $4 \mu\text{m}$ in three directions) compared to the voxel
 445 size ($0.12 \mu\text{m}$). The corresponding segmentation method relies on standard image processing
 446 operators including filtering, hysteresis thresholding and connected component filtering. In previous
 447 works, thresholding-based methods were also mainly proposed to segment lacunae from CLSM
 448 (Heveran et al., 2018) or micro-CT images (Hemmatian et al., 2017). Specific denoising operations
 449 were applied depending on the type of images and their spatial resolution. In our case, we did not
 450 used morphological operations (erosion and dilatation) to post process the images as in these
 451 previous works meaning that we kept the raw shape of the lacunae surface. Contrary to lacunae, the
 452 segmentation of canaliculi is more challenging and the methods to tackle it are hardly described in
 453 the previous works. Local or hysteresis thresholding were reported to segment the LCN from CLSM

454 images (Roschger *et al.*, 2019) or ptychographic images (Ciani *et al.*, 2018). Here, we investigated
455 more advanced segmentation methods based on variational region growing and geodesic voting,
456 which were both applied after a line-enhancement filter. Our results show that the region growing
457 method preserves better the connectivity and extracts more accurately the thickness of the canaliculi.
458 The geodesic voting method was developed to extract canaliculi path from CT images obtained at a
459 lower spatial resolution (voxel size 300 nm) (Zuluaga *et al.*, 2014). Compared to this situation, the
460 canaliculi may spread on more than one voxel in our case. In addition, the running time of the
461 geodesic voting method was much larger than that of the region growing and could become
462 prohibitive in some volumes. In conclusion, we selected the region growing method to segment
463 canaliculi considering its time-efficiency and efficacy to segment the entire volumes. The VRG
464 method including *vesselness* shape prior provides a general framework to segment network-type
465 structures made of nodes and branches that can be used beyond our application. A close approach
466 was for instance successfully demonstrated to segment vascular airways in lung CT images (Orkisz
467 *et al.*, 2014).

468 Our workflow includes a number of parameters to be set before running. The radius of the median
469 filter, the limit size of the connected components analysis and the standard deviation in the VRG are
470 related to the sizes of the anatomical structures of interest and were kept constant for all volumes.
471 The two thresholds of the hysteresis thresholding were selected according to the gray histogram of
472 the original image. Once these parameters are fixed, the workflow is totally automatic.

473 The quantification of the LCN was performed on eight human femoral cortical bone samples.
474 Each 3D volume contained on average 257 lacunae and the average density of lacunae was found to
475 be $24,000 \text{ mm}^{-3}$. The result of the density of lacunae is in the range of previous works $15,000\text{--}35,000$
476 mm^{-3} (Mader *et al.*, 2013, Bach-Gansmo *et al.*, 2016, Andronowski *et al.*, 2017, Gatti *et al.*, 2018).
477 Our study provided an estimation of the porosity of the LCN ($\frac{LCN.TV}{BV}$) of 1.12% including both the
478 lacunar porosity ($\frac{Lc.TV}{BV}$) and the canaliculi porosity ($\frac{Ca.TV}{BV}$). The 3D lacunar porosity 0.78% is in
479 agreement with that of previous research in our group using SR- μ CT 0.84% (Dong *et al.*, 2014a),
480 and that obtained from CSLM 0.68% (Repp *et al.*, 2017). There are very few reference values for the
481 canaliculi porosity in the literature. Here, it was found to be 0.37%, which is slightly smaller
482 compared to 0.57% in (Varga *et al.*, 2015). A value of 0.7% was reported in mice using FIB/SEM
483 but the calculation was limited to a very small region of interest (Schneider *et al.*, 2011), and 1.7–
484 1.9 % in rat tibias using CLSM (Gatti *et al.*, 2018) but in this case the values are likely to be
485 overestimated by the technique

486 We also obtained parameters describing the morphology and anisotropy of lacunae. We followed
487 an approach based on the second-order moment matrix of each shape in (Dong *et al.*, 2014a). It is
488 equivalent to the tensor-based approach proposed by (Mader *et al.*, 2013) using the covariance matrix
489 despite differences in notations (the order of eigenvalues is inverted). The same concept is used in
490 the work of (Heveran *et al.*, 2018) but they used the inertia matrix instead of the covariance matrix.
491 The stretch and oblateness were not computed but they can be straightforwardly recovered from the
492 ratios of the axis length $\frac{Lc.L_1}{Lc.L_2}$ and $\frac{Lc.L_2}{Lc.L_3}$. In this work, we also computed the four intrinsic volumes
493 including the volume, surface, mean curvature and Euler number of each lacunae. From a
494 mathematical point of view, these shape features are invariant under rigid transformations
495 (translations and rotations), additive and continuous. In addition, any shape feature having these

496 properties is a linear combination of these four intrinsic volumes (Ohser & Schladitz, 2009).. In this
497 sense these four intrinsic volumes are basic characteristics of a shape.”

498 The mean lacunar volume $Lc.V$ ($315.7 \mu\text{m}^3$) is consistent with previous reports ($\sim 50\text{--}730 \mu\text{m}^3$)
499 (Remaggi *et al.*, 1998, Carter *et al.*, 2013). Describing each lacuna as an equivalent ellipsoid, we got
500 the average lengths of the three axes. The calculated lengths, widths and depths are comparable with
501 previous works ($\sim 17 \mu\text{m}$, $9 \mu\text{m}$ and $4 \mu\text{m}$) and the ratio between them is about 4:2:1 (van Hove *et al.*
502 *et al.*, 2009, Dong *et al.*, 2014a). The average surface area $Lc.S$ is $323.3 \mu\text{m}^2$ which is consistent with
503 our previous work in human ($336.2 \mu\text{m}^2$) (van Hove *et al.*, 2009, Dong *et al.*, 2014a) and in the same
504 range as that reported in rats in (Heveran *et al.*, 2018). The average structure model index, around
505 3.1, did not show a large variability and was comparable with that reported in (Dong *et al.*, 2014a).

506 Moreover, we introduced some new parameters. The local porosity of the lacuna and canaliculi
507 was assessed by considering Voronoi cells associated to each lacuna. The average volume of each
508 Voronoi cell ($Cell.V$) was found to be $42,000 \mu\text{m}^3$, and represents in a way the volume of influence
509 of an osteocyte and its processes. The average volume of canaliculi per cell ($Ca.V$) was $139.3 \mu\text{m}^3$,
510 and the ratio $\frac{Lc.V}{Cell.V}$ (0.88%), $\frac{Ca.V}{Cell.V}$ (0.37%). The relative volume ratio of canaliculi to lacunae $\frac{Ca.V}{Lc.V}$ was
511 45.8%, which shows that the volume of canaliculi is approximately half that of lacuna. Here we did
512 not consider the truncation of the Voronoi cells due to the image boundaries. We expect that this
513 edge effect should have a limited impact with an average of about 259 lacunae per sample. These
514 parameters could help to assess the properties of the osteocyte system locally within their
515 environment. Besides, we found an average number of 58.2 primary canaliculi per lacunae, which
516 was smaller than that found in other studies but in rats and with other imaging techniques (Sharma
517 *et al.*, 2012, Ciani *et al.*, 2018).

518 We found some correlations between the measured parameters. For instance, the total lacunar
519 (resp canalicular) porosity was significantly correlated to the local lacunar (resp. canalicular)
520 porosity. The good correlation between $Cell.V$ and $\frac{Lc.N}{BV}$ can be explained by the dependency between
521 the division of Voronoi cells to the number of lacunae. Since the total volume imaged in each sample
522 is the same, the average volume of each Voronoi cell is smaller when containing more lacunae. There
523 was a strong correlation between the lacuna surface and its volume, which traduces some invariance
524 in the 3D ellipsoidal shape of the lacunae. The length of the long axis $Lc.L_1$. seems also to dominate
525 the geometry of the ellipsoid. The correlation between $\frac{Lc.L_2}{Lc.L_3}$ and $Lc.SMI$ traduces the fact that both
526 parameters are related to the anisotropy of the lacunae. Besides, there were good linear regressions
527 between $\frac{Lc.V}{Cell.V}$ and $\frac{Lc.TV}{BV}$, as well as $\frac{Ca.V}{Cell.V}$ and $\frac{Ca.TV}{BV}$. Nevertheless, since our data set is composed of
528 only eight samples, the results should be confirmed in further studies.

529 We acknowledge some limitations of this work. We used bone samples extracted from cadavers
530 but the medical history of the subject was not available. Nevertheless, this data set allowed us to
531 develop a framework that will be further used on more specific groups of samples to answer
532 dedicated medical questions on bone-related disease. In addition, due to the setup constraints, it was
533 difficult to select accurately a given zone in the sample for instance in osteonal tissue. Further work
534 could be done to analyze the properties of the LCN for instance in osteonal or interstitial tissue. Such
535 an analysis was performed from confocal laser scanning microscopy images (Repp *et al.*, 2017) or
536 from SR CT images at $0.7 \mu\text{m}$ (Gauthier *et al.*, 2019). However, such an analysis requires the
537 selection of osteonal regions for which there is currently no automatic image analysis procedure

538 available, and then remains time-consuming. Other methods could also be of interest to characterize
539 further the canaliculi network. In future, segmentation methods based on deep learning approaches
540 could also be investigated, which nevertheless poses the problem of having sufficient and reliable
541 annotated data sets.

542 In conclusion, the aim of this work was to present the complete method, going from data
543 acquisition at very high spatial resolution to the measurement of quantitative parameters of the LCN.
544 The imaging technique used here, magnified X-ray phase nano-CT, has the advantage to offer an
545 isotropic spatial resolution, sufficiently high for the observation of the canaliculi, while keeping a
546 large field of view including more than 250 lacunae per sample. Increasing the image magnification,
547 which is possible up to a voxel size ~30nm using X-ray phase nano-CT, could permit a better
548 assessment of canaliculi but at the expense of a smaller field of view. The proposed segmentation
549 method is quasi-automatic, efficient and compatible with the very large datasets in terms of
550 computation time and resources. We calculate 3D quantitative parameters on the entire volumes
551 instead of cropped sub-volumes as it was generally done previously. Consequently, the values
552 reported here for the density, the porosity and the morphology of the lacunae and canaliculi are more
553 statistically representative. The data processing workflow provides a framework that could possibly
554 be transposable to other 3D imaging modalities (like optical imaging), provided that the parameters
555 of the method are adapted. This work then opens many perspectives to have a better insight on the
556 LCN in pathological and healthy bone, both in human and animal models, and is expected to
557 contribute to a better understanding of the mechanisms of bone fragility.

558 **Acknowledgements**

559 This work was done in the framework of LabEx PRIMES ANR-11-LABX-006 of Université de Lyon
560 and in the context of the ANR MULTIPS project (ANR-13-BS09-0006). We thank the ESRF for
561 providing access to beamtime and support through the Long Term Proposal MD830. The authors
562 acknowledge H  l  ne Follet (Lyos, Lyon), R  my Gauthier (Turin, Italy) and David Mitton for sample
563 preparation. We also express our gratitude to Pierre Jean Gouttenoire for assistance in computer
564 programming.

565 **References**

- 566 Andronowski, J. M., Mundorff, A. Z., Pratt, I. V., Davoren, J. M. & Cooper, D. M. L. (2017)
567 Evaluating differential nuclear DNA yield rates and osteocyte numbers among human bone
568 tissue types: A synchrotron radiation micro-CT approach. *Forensic Science International:
569 Genetics*, **28**, 211-218.
- 570 Bach-Gansmo, F. L., Br  iel, A., Jensen, M. V., Ebbesen, E. N., Birkedal, H. & Thomsen, J. S. (2016)
571 Osteocyte lacunar properties and cortical microstructure in human iliac crest as a function of
572 age and sex. *Bone*, **91**, 11-19.
- 573 Bonewald, L. F. (2011) The amazing osteocyte. *Journal of Bone and Mineral Research*, **26**, 229-
574 238.
- 575 Buenzli, P. R. & Sims, N. A. (2015) Quantifying the osteocyte network in the human skeleton. *Bone*,
576 **75**, 144-150.
- 577 Cai, X., Peralta, L., Giron, A., Helfen, L., Olivier, C., Peyrin, F., Laugier, P. & Grimal, Q. (2017)
578 Cortical bone elasticity measured by resonant ultrasound spectroscopy is not altered by
579 defatting and synchrotron X-ray imaging. *Journal of the Mechanical Behavior of Biomedical
580 Materials*, **72**, 241-245.

581 Carter, Y., Thomas, C. D. L., Clement, J. G. & Cooper, D. M. L. (2013) Femoral osteocyte lacunar
582 density, volume and morphology in women across the lifespan. *Journal of Structural*
583 *Biology*, **183**, 519-526.

584 Chan, T. F. & Vese, L. A. (2001) Active contours without edges. *IEEE Transactions on Image*
585 *Processing*, **10**, 266-277.

586 Ciani, A., Guizar-Sicairos, M., Diaz, A., Holler, M., Pallu, S., Achiou, Z., Jennane, R., Toumi, H.,
587 Lespessailles, E. & Kewish, C. (2016) Segmentation of nanotomographic cortical bone
588 images for quantitative characterization of the osteocyte lacuno-canalicular network. In: *AIP*
589 *Conference Proceedings*. AIP Publishing LLC.

590 Ciani, A., Toumi, H., Pallu, S., Tsai, E. H. R., Diaz, A., Guizar-Sicairos, M., Holler, M.,
591 Lespessailles, E. & Kewish, C. M. (2018) Ptychographic X-ray CT characterization of the
592 osteocyte lacuno-canalicular network in a male rat's glucocorticoid induced osteoporosis
593 model. *Bone Reports*, **9**, 122-131.

594 Currey JD. (2005), Bone architecture and fracture. *Current Osteoporosis Reports*. 2005 **3**, 52-56.

595 Dierolf, M., Menzel, A., Thibault, P., Schneider, P., Kewish, C. M., Wepf, R., Bunk, O. & Pfeiffer,
596 F. (2010) Ptychographic X-ray computed tomography at the nanoscale. *Nature*, **467**, 436-
597 439.

598 Dong, P., Hauptert, S., Hesse, B., Langer, M., Gouttenoire, P.-J., Bousson, V. & Peyrin, F. (2014a)
599 3D osteocyte lacunar morphometric properties and distributions in human femoral cortical
600 bone using synchrotron radiation micro-CT images. *Bone*, **60**, 172-185.

601 Dong, P., Pacureauu, A., Zuluaga, M. A., Olivier, C., Grimal, Q. & Peyrin, F. (2014b) Quantification
602 of the 3D morphology of the bone cell network from synchrotron micro-CT images. *Image*
603 *Analysis & Stereology*, **33**, 157-166.

604 Florencio-Silva, R., Sasso, G. R. d. S., Sasso-Cerri, E., Simões, M. J. & Cerri, P. S. (2015) Biology
605 of Bone Tissue: Structure, Function, and Factors That Influence Bone Cells. *BioMed*
606 *Research International*, **2015**:421746.

607 Gatti, V., Azoulay, E. M. & Fritton, S. P. (2018) Microstructural changes associated with
608 osteoporosis negatively affect loading-induced fluid flow around osteocytes in cortical bone.
609 *Journal of Biomechanics*, **66**, 127-136.

610 Gauthier, R., Follet, H., Olivier, C., Mitton, D. & Peyrin, F. (2019) 3D analysis of the osteonal and
611 interstitial tissue in human radii cortical bone. *Bone*, **127**, 526-536.

612 Genthial, R., Beaurepaire, E., Schanne-Klein, M.-C., Peyrin, F., Farlay, D., Olivier, C., Bala, Y.,
613 Boivin, G., Vial, J.-C., Débarre, D. & Gourrier, A. (2017) Label-free imaging of bone
614 multiscale porosity and interfaces using third-harmonic generation microscopy. *Scientific*
615 *Reports*, **7**, 3419.

616 Hemmatian, H., Laurent, M. R., Ghazanfari, S., Vanderschueren, D., Bakker, A. D., Klein-Nulend,
617 J. & van Lenthe, G. H. (2017) Accuracy and reproducibility of mouse cortical bone
618 microporosity as quantified by desktop microcomputed tomography. *PLOS ONE*, **12**,
619 e0182996.

620 Heveran, C. M., Rauff, A., King, K. B., Carpenter, R. D. & Ferguson, V. L. (2018) A new open-
621 source tool for measuring 3D osteocyte lacunar geometries from confocal laser scanning
622 microscopy reveals age-related changes to lacunar size and shape in cortical mouse bone.
623 *Bone*, **110**, 115-127.

624 Hubert, M., Pacureauu, A., Guilloud, C., Yang, Y., da Silva, J. C., Laurencin, J., Lefebvre-Joud, F.
625 & Cloetens, P. (2018) Efficient correction of wavefront inhomogeneities in X-ray
626 holographic nanotomography by random sample displacement. *Applied Physics Letters*, **112**,
627 203704.

628 Jehan-Besson, S., Barlaud, M. & Aubert, G. (2003) DREAM2S: Deformable Regions Driven by an
629 Eulerian Accurate Minimization Method for Image and Video Segmentation. *International*
630 *Journal of Computer Vision*, **53**, 45-70.

631 Jilka, R. L. & O'Brien, C. A. (2016) The Role of Osteocytes in Age-Related Bone Loss. *Current*
632 *Osteoporosis Reports*, **14**, 16-25.

633 Joeng, K. S., Lee, Y.-C., Lim, J., Chen, Y., Jiang, M.-M., Munivez, E., Ambrose, C. & Lee, B. H.
634 (2017) Osteocyte-specific WNT1 regulates osteoblast function during bone homeostasis.
635 *Journal of Clinical Investigation*, **127**, 2678-2688.

636 Jordan, G. R., Loveridge, N., Power, J., Clarke, M. T., Parker, M. & Reeve, J. (2003) The Ratio of
637 Osteocytic Incorporation to Bone Matrix Formation in Femoral Neck Cancellous Bone: An
638 Enhanced Osteoblast Work Rate in the Vicinity of Hip Osteoarthritis. *Calcified Tissue*
639 *International*, **72**, 190-196.

640 Kamel-ElSayed, S. A., Tiede-Lewis, L. M., Lu, Y., Veno, P. A. & Dallas, S. L. (2015) Novel
641 approaches for two and three dimensional multiplexed imaging of osteocytes. *Bone*, **76**, 129-
642 140.

643 Kamioka, H., Honjo, T. & Takano-Yamamoto, T. (2001) A three-dimensional distribution of
644 osteocyte processes revealed by the combination of confocal laser scanning microscopy and
645 differential interference contrast microscopy. *Bone*, **28**, 145-149.

646 Kanis, J. A., Harvey, N. C., Cooper, C., Johansson, H., Odén, A. & McCloskey, E. V. (2016) A
647 systematic review of intervention thresholds based on FRAX: A report prepared for the
648 National Osteoporosis Guideline Group and the International Osteoporosis Foundation.
649 *Archives of Osteoporosis*, **11**, 1-25.

650 Knothe Tate, M. L., Adamson, J. R., Tami, A. E. & Bauer, T. W. (2004) The osteocyte. *The*
651 *International Journal of Biochemistry & Cell Biology*, **36**, 1-8.

652 Kollmannsberger, P., Kerschnitzki, M., Repp, F., Wagermaier, W., Weinkamer, R. & Fratzl, P.
653 (2017) The small world of osteocytes: connectomics of the lacuno-canalicular network in
654 bone. *New Journal of Physics*, **19**, 073019.

655 Langer, M., Pacureanu, A., Suhonen, H., Grimal, Q., Cloetens, P. & Peyrin, F. (2012) X-Ray Phase
656 Nanotomography Resolves the 3D Human Bone Ultrastructure. *PLoS ONE*, **7**, e35691.

657 Lesage, D., Angelini, E. D., Bloch, I. & Funke-Lea, G. (2009) A review of 3D vessel lumen
658 segmentation techniques: Models, features and extraction schemes. *Medical Image Analysis*,
659 **13**, 819-845.

660 Mader, K. S., Schneider, P., Müller, R. & Stämpfli, M. (2013) A quantitative framework for the
661 3D characterization of the osteocyte lacunar system. *Bone*, **57**, 142-154.

662 Marotti, G., Ferretti, M., Remaggi, F. & Palumbo, C. (1995) Quantitative evaluation on osteocyte
663 canalicular density in human secondary osteons. *Bone*, **16**, 125-128.

664 Mirone, A., Brun, E., Gouillart, E., Tafforeau, P. & Kieffer, J. (2014) The PyHST2 hybrid distributed
665 code for high speed tomographic reconstruction with iterative reconstruction and a priori
666 knowledge capabilities. *Nuclear Instruments and Methods in Physics Research Section B:*
667 *Beam Interactions with Materials and Atoms*, **324**, 41-48.

668 Moccia, S., De Momi, E., El Hadji, S. & Mattos, L. S. (2018) Blood vessel segmentation algorithms
669 — Review of methods, datasets and evaluation metrics. *Computer Methods and Programs in*
670 *Biomedicine*, **158**, 71-91.

671 Ohser, J. & Schlodtz, K. (2009) *3D images of materials structures: processing and analysis*, John
672 Wiley & Sons.

673 Orkisz, M., Hernández Hoyos, M., Pérez Romanello, V., Pérez Romanello, C., Prieto, J. C. & Revol-
674 Muller, C. (2014) Segmentation of the pulmonary vascular trees in 3D CT images using
675 variational region-growing. *IRBM*, **35**, 11-19.

676 Pacureanu, A., Langer, M., Boller, E., Tafforeau, P. & Peyrin, F. o. (2012) Nanoscale imaging of the
677 bone cell network with synchrotron X-ray tomography: optimization of acquisition setup:
678 Synchrotron x-ray tomography reveals the bone cell network. *Medical Physics*, **39**, 2229-
679 2238.

680 Pacureanu, A., Revol-Muller, C., Rose, J.-L., Ruiz, M. S. & Peyrin, F. (2010) Vesselness-guided
681 variational segmentation of cellular networks from 3D micro-CT. In: *2010 IEEE*
682 *International Symposium on Biomedical Imaging: From Nano to Macro*. IEEE, 912-915

683 Pacureanu, A. J. (2012) Imaging the bone cell network with nanoscale synchrotron computed
684 tomography. INSA de Lyon.

685 Qiu, S., Rao, D. S., Palnitkar, S. & Parfitt, A. M. (2006) Differences in osteocyte and lacunar density
686 between Black and White American women. *Bone*, **38**, 130-135.

687 Remaggi, F., Canè, V., Palumbo, C. & Ferretti, M. (1998) Histomorphometric study on the osteocyte
688 lacuno-canalicular network in animals of different species. I. Woven-fibered and parallel-
689 fibered bones. *Italian Journal of Anatomy and Embryology = Archivio Italiano Di Anatomia*
690 *Ed Embriologia*, **103**, 145-155.

691 Repp, F., Kollmannsberger, P., Roschger, A., Kerschnitzki, M., Berzlanovich, A., Gruber, G. M.,
692 Roschger, P., Wagermaier, W. & Weinkamer, R. (2017) Spatial heterogeneity in the
693 canalicular density of the osteocyte network in human osteons. *Bone Reports*, **6**, 101-108.

694 Rho, J.-Y., Kuhn-Spearing, L. & Zioupos, P. (1998) Mechanical properties and the hierarchical
695 structure of bone. *Medical Engineering & Physics*, **20**, 92-102.

696 Roschger, A., Roschger, P., Wagermaier, W., Chen, J., van Tol, A. F., Repp, F., Blouin, S.,
697 Berzlanovich, A., Gruber, G. M., Klaushofer, K., Fratzl, P. & Weinkamer, R. (2019) The
698 contribution of the pericanalicular matrix to mineral content in human osteonal bone. *Bone*,
699 **123**, 76-85.

700 Rose, J.-L., Grenier, T., Revol-Muller, C. & Odet, C. (2010) Unifying variational approach and
701 region growing segmentation. In: *2010 18th European Signal Processing Conference*. IEEE,
702 1781-1785.

703 Rubin, M. A. & Jasiuk, I. (2005) The TEM characterization of the lamellar structure of osteoporotic
704 human trabecular bone. *Micron*, **36**, 653-664.

705 Sahoo, P. K., Soltani, S. & Wong, A. K. C. (1988) A survey of thresholding techniques. *Computer*
706 *Vision, Graphics, and Image Processing*, **41**, 233-260.

707 Sato, Y., Nakajima, S., Shiraga, N., Atsumi, H., Yoshida, S., Koller, T., Gerig, G. & Kikinis, R.
708 (1998) Three-dimensional multi-scale line filter for segmentation and visualization of
709 curvilinear structures in medical images. *Medical Image Analysis*, **2**, 143-168.

710 Schneider, P., Meier, M., Wepf, R. & Müller, R. (2011) Serial FIB/SEM imaging for quantitative 3D
711 assessment of the osteocyte lacuno-canalicular network. *Bone*, **49**, 304-311.

712 Shah, F. A. & Palmquist, A. (2017) Evidence that Osteocytes in Autogenous Bone Fragments can
713 Repair Disrupted Canalicular Networks and Connect with Osteocytes in de novo Formed
714 Bone on the Fragment Surface. *Calcified Tissue International*, **101**, 321-327.

715 Sharma, D., Ciani, C., Marin, P. A. R., Levy, J. D., Doty, S. B. & Fritton, S. P. (2012) Alterations
716 in the osteocyte lacunar–canalicular microenvironment due to estrogen deficiency. *Bone*, **51**,
717 488-497.

718 van Hove, R. P., Nolte, P. A., Vatsa, A., Semeins, C. M., Salmon, P. L., Smit, T. H. & Klein-Nulend,
719 J. (2009) Osteocyte morphology in human tibiae of different bone pathologies with different
720 bone mineral density — Is there a role for mechanosensing? *Bone*, **45**, 321-329.

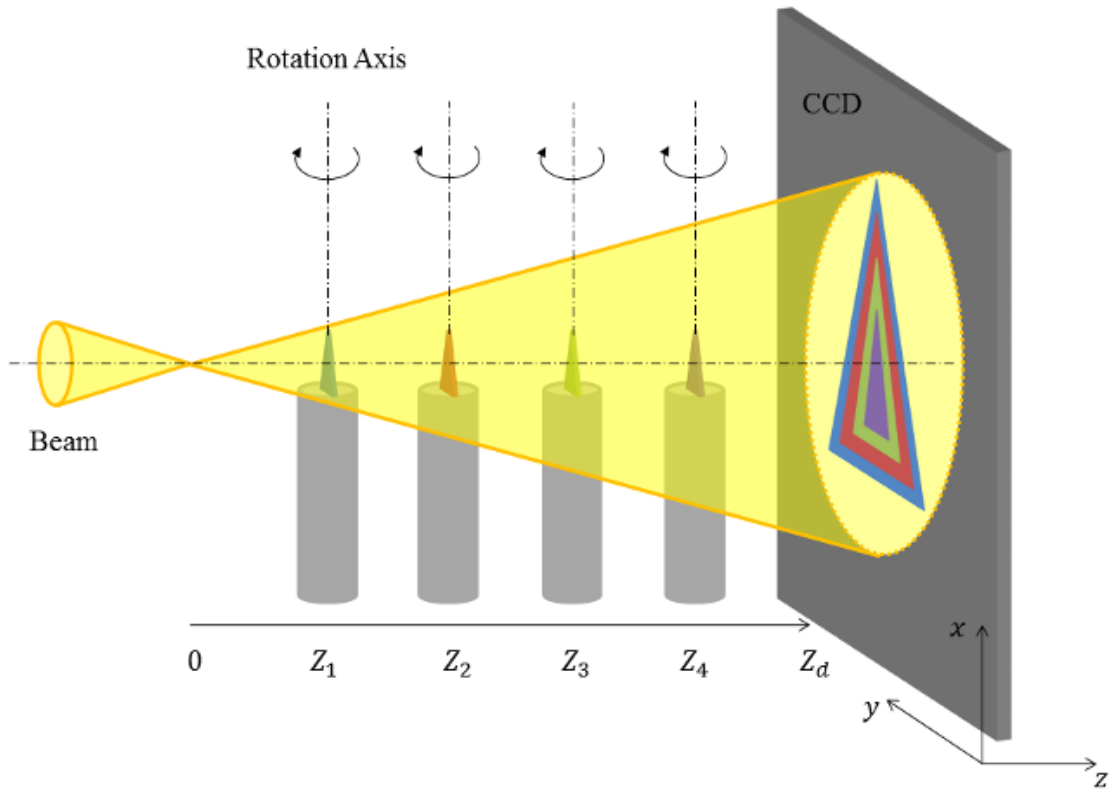
721 Varga, P., Hesse, B., Langer, M., Schrof, S., Männicke, N., Suhonen, H., Pacureanu, A., Pahr, D.,
722 Peyrin, F. & Raum, K. (2015) Synchrotron X-ray phase nano-tomography-based analysis of
723 the lacunar–canalicular network morphology and its relation to the strains experienced by
724 osteocytes in situ as predicted by case-specific finite element analysis. *Biomechanics and*
725 *Modeling in Mechanobiology*, **14**, 267-282.

726 Villar, F., Andre, L., Baker, R., Bohic, S., da Silva, J., Guilloud, C., Hignette, O., Meyer, J.,
727 Pacureanu, A. & Perez, M. (2018) Nanopositioning for the ESRF ID16a nano-imaging
728 beamline. *Synchrotron Radiation News*, **31**, 9-14.

729 Yu, B., Weber, L., Pacureanu, A., Langer, M., Olivier, C., Cloetens, P. & Peyrin, F. (2018)
730 Evaluation of phase retrieval approaches in magnified X-ray phase nano computerized
731 tomography applied to bone tissue. *Optics Express*, **26**, 11110.
732 Zebaze, R. M. D., Ghasem-Zadeh, A., Bohte, A., Iuliano-Burns, S., Mirams, M., Price, R. I., Mackie,
733 E. J. & Seeman, E. (2010) Intracortical remodelling and porosity in the distal radius and post-
734 mortem femurs of women: a cross-sectional study. *The Lancet*, **375**, 1729-1736.
735 Zhu, S. C. & Yuille, A. (1996) Region competition: unifying snakes, region growing, and
736 Bayes/MDL for multiband image segmentation. *IEEE Transactions on Pattern Analysis and*
737 *Machine Intelligence*, **18**, 884-900.
738 Zuluaga, M. A., Orkisz, M., Dong, P., Pacureanu, A., Gouttenoire, P.-J. & Peyrin, F. (2014) Bone
739 canalicular network segmentation in 3D nano-CT images through geodesic voting and image
740 tessellation. *Physics in Medicine and Biology*, **59**, 2155–2171
741
742

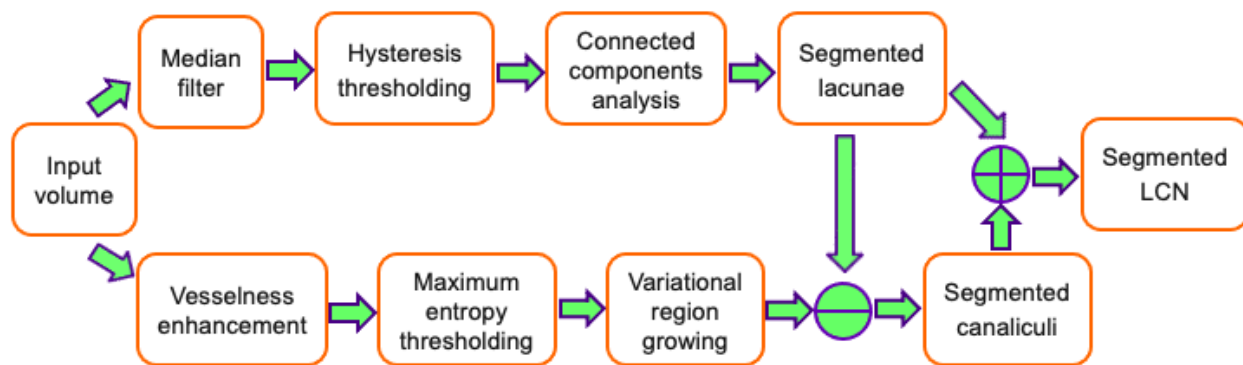
743 **Figure Captions**

- 744
745 Figure 1: Illustration of the image acquisition in X-ray phase nano-CT : the CT scanning of the
746 sample is sequentially repeated at 4 different focus-to-sample distances Z_1 , Z_2 , Z_3 and Z_4 (Yu et al.,
747 2018)
748
749 Figure 2: Workflow for the segmentation of the LCN. The top line corresponds to the segmentation
750 of lacunae and the bottom one to that of canaliculi.
751
752 Figure 3: Segmentation of the canaliculi in the 3D volume, illustrated by MIPs of 256 slices along
753 the Z-axis. (a) MIP of the original volume; (b) MIP of the result after vesselness enhancement; (c)
754 MIP of the seed map after maximum entropy thresholding; (d) MIP after variational region growing
755 including segmented lacunae and canaliculi; (e) MIP of the segmented canaliculi
756
757 Figure 4: 3D Voronoi tessellation. (a) A slice from the original volume; (b) The corresponding slice
758 in the 3D Voronoi tessellation image; (c) An overlay of (a) and (b)
759
760 Figure 5: Results of the VRG method around three lacunae; (a)-(d)-(h): MIPs along the Z-axis of the
761 original sub volume at 120 nm; (b)-(e)-(i): MIPs of the corresponding image segmented by the
762 maximum entropy thresholding; (c)-(f)-(j): MIPs of the segmented image after variational region
763 growing
764
765 Figure 6: Comparison of VRG and geodesic voting, illustrated by MIPs of 128 slices along the Z-
766 axis. (a) MIP of the original volume; (b) MIP of the segmented LCN by variational region growth;
767 (c) MIP of the segmented LCN by geodesic voting; (d), (e) and (f) zoomed MIPs on the red square
768 regions corresponding to (a), (b) and (c) respectively.
769
770 Figure 7: Segmentation results for the sample A2. (a) MIP along the Y-axis of 100 middle slices
771 from the reconstructed volume; (b) 3D rendering of the segmented lacunae (yellow) and canaliculi
772 (green). The white spot corresponds to a Haversian canal.
773
774
775
776
777
778



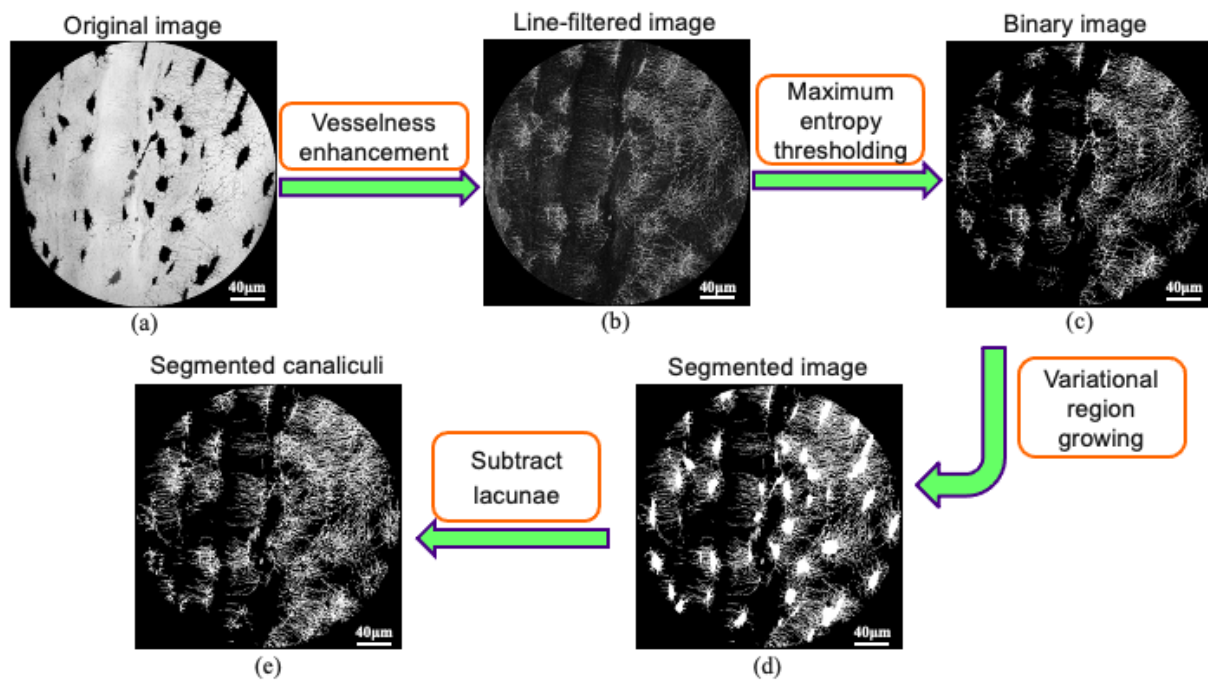
769

770 Fig1



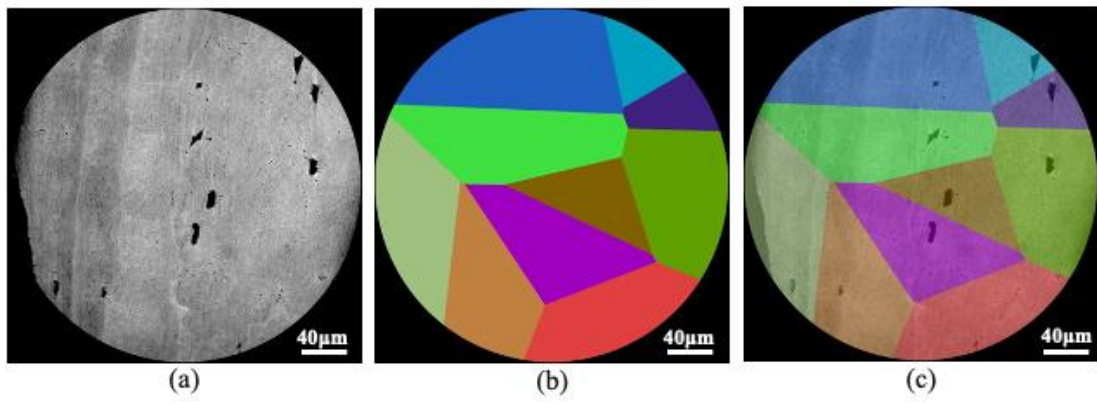
771

772 Fig2



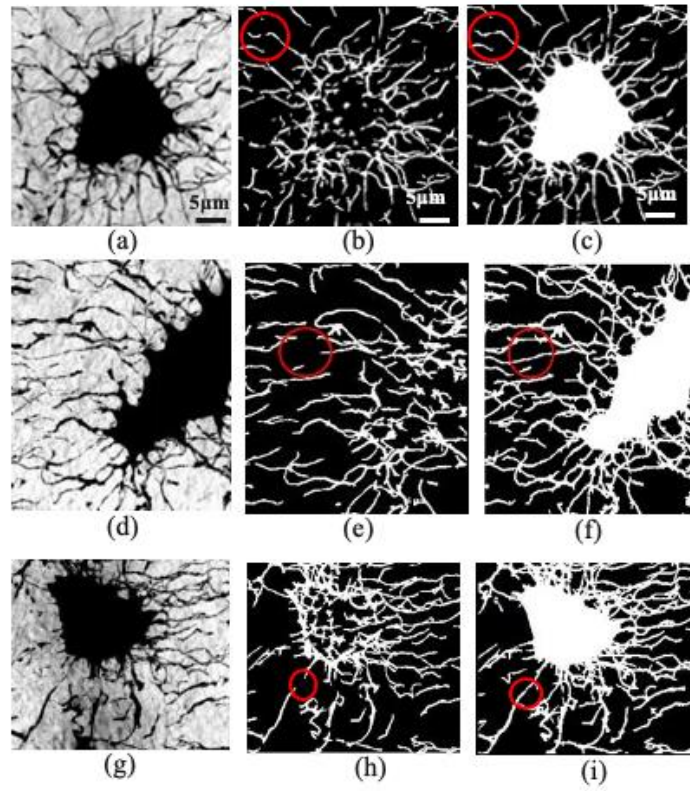
773

774 Fig3



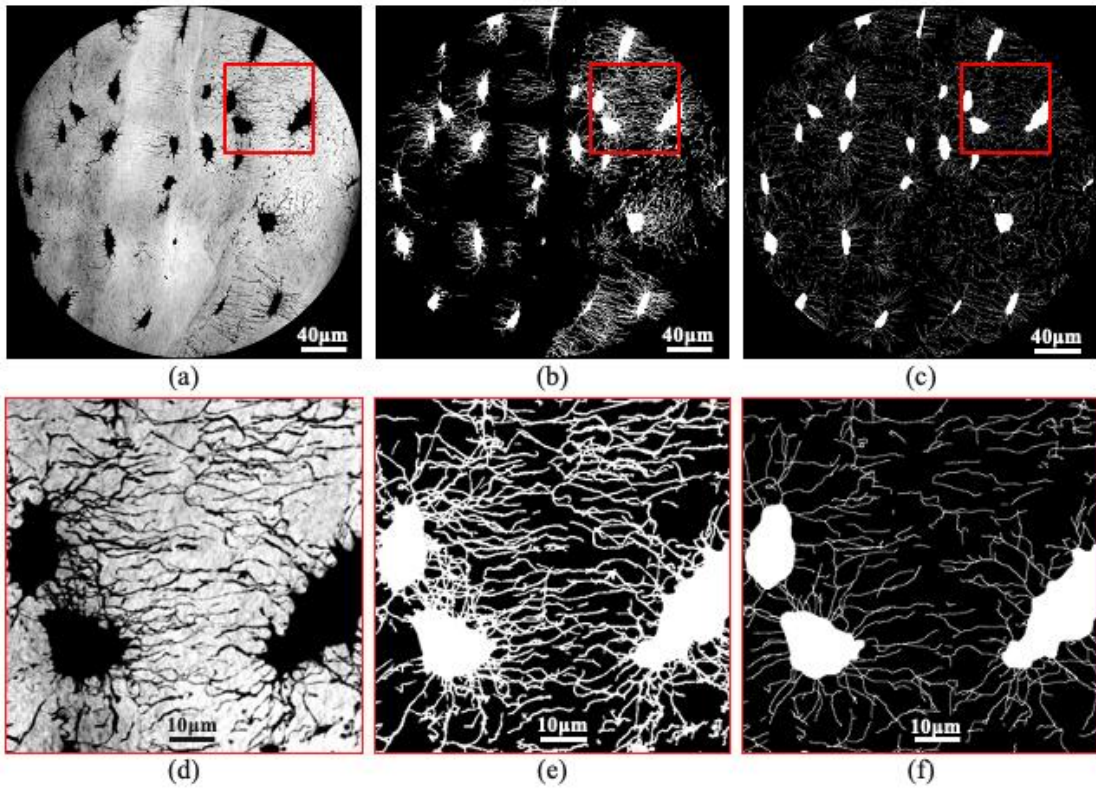
775

776 Fig4



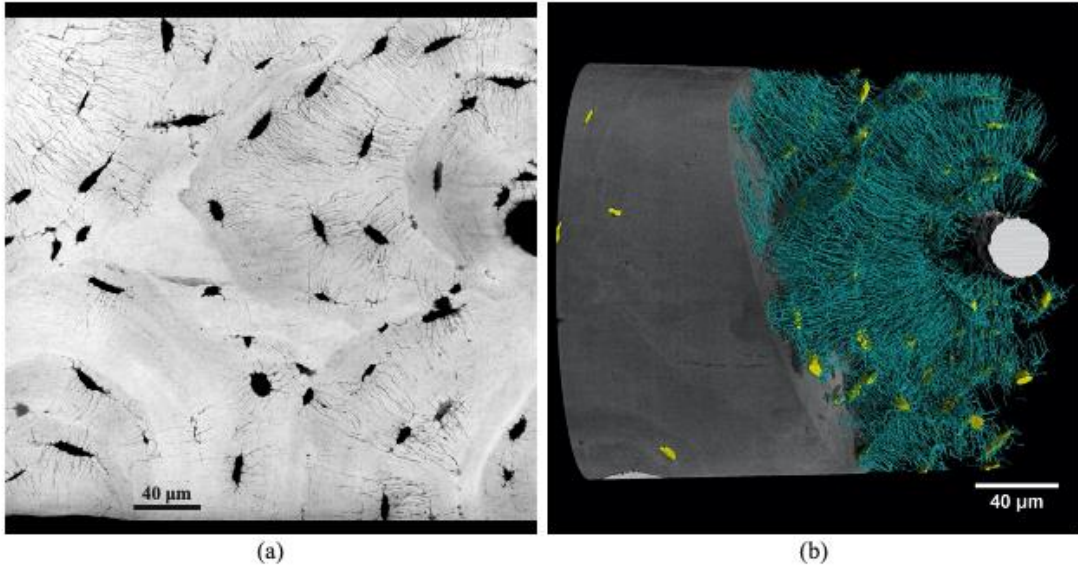
777

778 Fig5

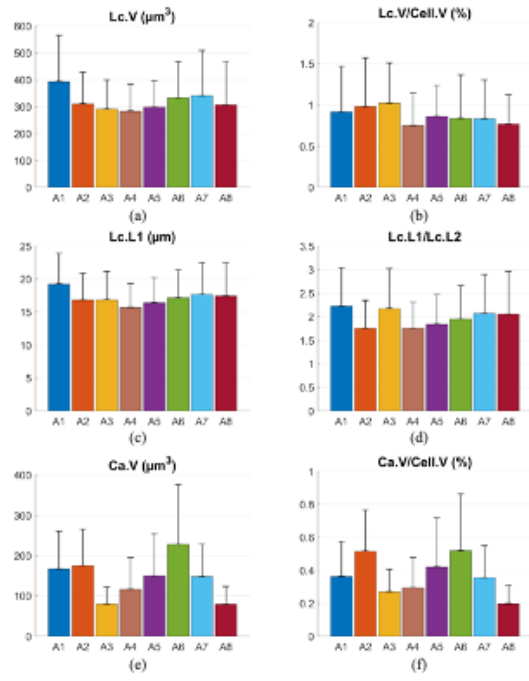


779

780 Fig6



781 Fig7
782
783



784

785 Fig8

8